

# The plasmon Talbot effect

Mark R. Dennis,<sup>1</sup> Nikolay I. Zheludev,<sup>2</sup> and F. Javier García de Abajo<sup>3\*1</sup>

<sup>1</sup>*School of Mathematics, University of Southampton, Southampton SO17 1BJ, UK*

<sup>2</sup>*Optoelectronics Research Center, University of Southampton, Southampton SO17 1BJ, UK*

<sup>3</sup>*Instituto de Óptica, CSIC, Serrano 121, 28006 Madrid, Spain*

\*Corresponding author: jga@io.cfmac.csic.es

The plasmon analog of the self-imaging Talbot effect is described and theoretically analyzed. Rich plasmon carpets containing hot spots are shown to be produced by a row of periodically-spaced surface features. A row of holes drilled in a metal film and illuminated from the back side is discussed as a realizable implementation of this concept. Self-images of the row are produced, separated from the original one by distances up to several hundreds of wavelengths in the examples under consideration. The size of the image focal spots is close to half a wavelength and the spot positions can be controlled by changing the incidence direction of external illumination, suggesting the possibility of using this effect (and its extension to non-periodic surface features) for far-field patterning and for long-distance plasmon-based interconnects in plasmonic circuits, energy transfer, and related phenomena.

## INTRODUCTION

An important aspect in the development of new branches of optics is the study of analogues of classical optical phenomena. In the field of surface waves on metals (surface plasmons) this approach has successfully met with engineered nanoscale features providing analogues of lenses and mirrors for future plasmon-based devices [1, 2, 3]. Such manipulation of surface plasmons is of much interest, both from a fundamental viewpoint [1] and from a view to applications [2, 3]. In practice, it is more difficult to manipulate plasmon fields than their free-space counterparts, as they are highly sensitive to metal surface imperfections on the scale of the skin depth ( $\sim 15$  nm); nevertheless, they have certain advantages, like their ability to concentrate the electromagnetic field near the surface, thus providing a route towards compact light waveguides [4], or their capacity to unveil Raman emission from single molecules through enhancement of the local field intensity by several orders of magnitude with respect to the incident light [5]. Here, we describe and theoretically analyze the plasmon analogue to another well-known phenomenon of classical optics, namely the self-imaging effect discovered by Talbot in 1836 [6] while studying transmission gratings and arrays of holes perforated in metal films, and later rediscovered and explained by Lord Rayleigh [7, 8]. The effect is best observed through the formation of repeated monochromatic images of a grating at various characteristic distances of the image plane with respect to the grating surface.

More precisely, a transversally periodic field, paraxially propagating, *revives* (self-images) to its initial configuration after the *Talbot distance*  $\tau = 2a^2/\lambda$ , where  $a$  is the transverse period and  $\lambda$  is the wavelength. In a simple analytical description, we represent the grating by a periodic function given in Fourier series form,

$$f(x, 0) = \sum_m f_m \exp(i2\pi mx/a),$$

where  $x$  is the direction of periodicity. The monochromatic wave function emanating from the grating towards the  $y$  direction reduces then to

$$f(x, y) = \sum_m f_m \exp(i2\pi mx/a) \exp(i2\pi \zeta_m y/\lambda), \quad (1)$$

where  $\zeta_m = \sqrt{1 - (m\lambda/a)^2}$ . The coefficients of  $x$  and  $y$  in these exponential functions define a vector of magnitude  $2\pi/\lambda$ , the light momentum. In the paraxial approximation ( $\lambda \ll a$ ), the binomial expansion

$$\zeta_m/\lambda = \frac{1}{\lambda} - \frac{m^2}{\tau} - \left(\frac{\lambda}{a}\right)^2 \frac{m^4}{4\tau} - \left(\frac{\lambda}{a}\right)^4 \frac{m^6}{8\tau} - \dots \quad (2)$$

can be truncated at the term proportional to  $m^2$ , equivalent to Fresnel diffraction. This yields

$$f(x, y) \approx \exp(i2\pi y/\lambda) \sum_m f_m \exp(i2\pi mx/a) \exp(-i2\pi m^2 y/\tau), \quad (3)$$

from where we immediately deduce

$$f(x, \tau) \approx \exp(i2\pi y/\lambda) f(x, 0), \quad (4)$$

$$f(x, \tau/2) \approx \exp(i2\pi y/\lambda) f(x - a/2, 0). \quad (5)$$

The length  $\tau = 2a^2/\lambda$  is indeed the Talbot distance at which the initial field self-images (except for an overall phase that is washed away when observing intensities), while another image is formed at  $\tau/2$ , laterally shifted by half a period and leading to an alternate definition of the Talbot distance [9]. When  $y$  is a fraction of  $\tau$ , the field undergoes *fractional revivals*, which in the ideal case are fractal at irrational values of  $y/\tau$  [9, 10, 11]. This exotic behavior is a consequence of Gauss sums arising from paraxial propagation, which relies on the smallness of the non-paraxiality parameter  $\lambda/a$ . In practice, this approximation stands only for a finite number of  $m$ 's in (1), but it can be sufficient to render well-defined focal spots, as we shall see below for self-imaging of small features.

The Talbot effect has been studied in a variety of theoretical and experimental situations [9, 10, 11, 12, 13]. This phenomenon has an analogue in Schrödinger evolution of quantum mechanical wavepackets, the quantum and fractional revivals of which have been thoroughly discussed [14, 15]. Although revivals are an exact consequence of quantum mechanics, they only arise in optics under the paraxial approximation, and deviation from paraxiality destroys the sensitive structure of the Talbot revivals [9]. However, non-paraxial propagation, which only involves a finite number of propagating waves, exhibits some good but approximate self-imaging near the paraxial Talbot distance [16, 17].

Self-imaging is not exclusive of periodic objects. The Montgomery effect [18, 19] describes for instance perfect image reconstruction of aperiodic objects made of incommensurate harmonic components  $\exp[i2\pi(m/\sqrt{|m|})x/a]$ , leading to replacement of  $|m|$  for  $m^2$  in Eq. (3), and obviously maintaining the property (4), but not (5). Recent work on a metal film perforated by quasiperiodic hole arrays has also revealed concentration of transmitted light intensity in hot spots at large distances from the film [20], suggesting possible extensions of the plasmon Talbot effect to aperiodic distributions of surface features.

## SELF-FOCUSING OF PLASMON CARPETS ON METALS: THE PLASMON TALBOT EFFECT

The analog of the Talbot effect using plasmons is illustrated in Fig. 1. A light plane wave is incident from the back of a metal film, planar except for a periodic one-dimensional array of nanoholes or other subwavelength structures, with period  $a$ . Light is partly transmitted into plasmons on the exit side of the film, thus deploying a complex carpet pattern. The field from each of the nanoholes is modeled as a dipole, oscillating with a frequency corresponding to the incident wavelength  $\lambda_0$ . This oscillation sets up surface plasmons, propagating into the plasmonic far-field with wavelength  $\lambda_{\text{SP}} = \lambda_0/\Re\{\sqrt{\epsilon/(1+\epsilon)}\}$ , which depends on the particular frequency-dependent dielectric function  $\epsilon$  of the metal. We shall concentrate our description on the situation most likely to find practical application, with small attenuation and  $|\epsilon| \gg 1$ , implying that  $\lambda_{\text{SP}} \approx \lambda_0$ . We shall also concentrate on values of the periodicity  $a$  of similar lengthscale to the plasmon wavelength  $\lambda_{\text{SP}}$ . In our graphical illustrations, we model a silver surface with incident wavelength  $\lambda_0 = 1.55 \mu\text{m}$ , for which  $\epsilon = -130.83 + i3.32$  [21], giving  $\lambda_{\text{SP}} = 1.544 \mu\text{m}$ .

Our detailed analysis starts with the field due to an oscillating single dipole in the  $y$  direction at position  $\mathbf{R}_0$  infinitesimally close to the metal surface, incorporating direct propagation and reflection. The electric field, made dimensionless through multiplication by  $\lambda_0^3$ , reads [22]

$$\mathbf{E}_{\text{single}}(\mathbf{r}) = \int d^2\mathbf{Q} \exp[i\mathbf{k} \cdot (\mathbf{r} - \mathbf{R}_0)] \mathbf{F}(\mathbf{Q}), \quad (6)$$

where

$$\mathbf{F}(\mathbf{Q}) = \frac{i\lambda_0^2}{Qk_z} [\hat{\mathbf{e}}_p k_z k_y (1 - r_p) + \hat{\mathbf{e}}_s k k_x (1 + r_s)], \quad (7)$$

$k = 2\pi/\lambda_0$  is the free-space light momentum,  $\mathbf{Q} = (k_x, k_y)$  is the projection of the wavevector  $\mathbf{k}$  into the plane of the metal,  $k_z = \sqrt{k^2 - Q^2}$  is the component normal to that plane,  $\{\hat{\mathbf{k}}, \hat{\mathbf{e}}_p, \hat{\mathbf{e}}_s\}$  is the natural orthonormal basis for  $\mathbf{k}$ , defined as  $\hat{\mathbf{e}}_s = \hat{\mathbf{z}} \times \hat{\mathbf{k}}/|\hat{\mathbf{z}} \times \hat{\mathbf{k}}|$  and  $\hat{\mathbf{e}}_p = \hat{\mathbf{e}}_s \times \hat{\mathbf{k}}$ , and  $r_p = (\epsilon k_z - k'_z)/(\epsilon k_z + k'_z)$  and  $r_s = (k_z - k'_z)/(k_z + k'_z)$  are the appropriate Fresnel reflection coefficients for TM ( $p$ ) and TE ( $s$ ) polarization, with  $k'_z = \sqrt{k^2\epsilon - Q^2}$  [23]. The dominant component to  $\mathbf{E}_{\text{single}}$  is  $E_z$ , and this is strongest on the metal plane for  $\mathbf{r} - \mathbf{R}_0$  in the direction of the dipole

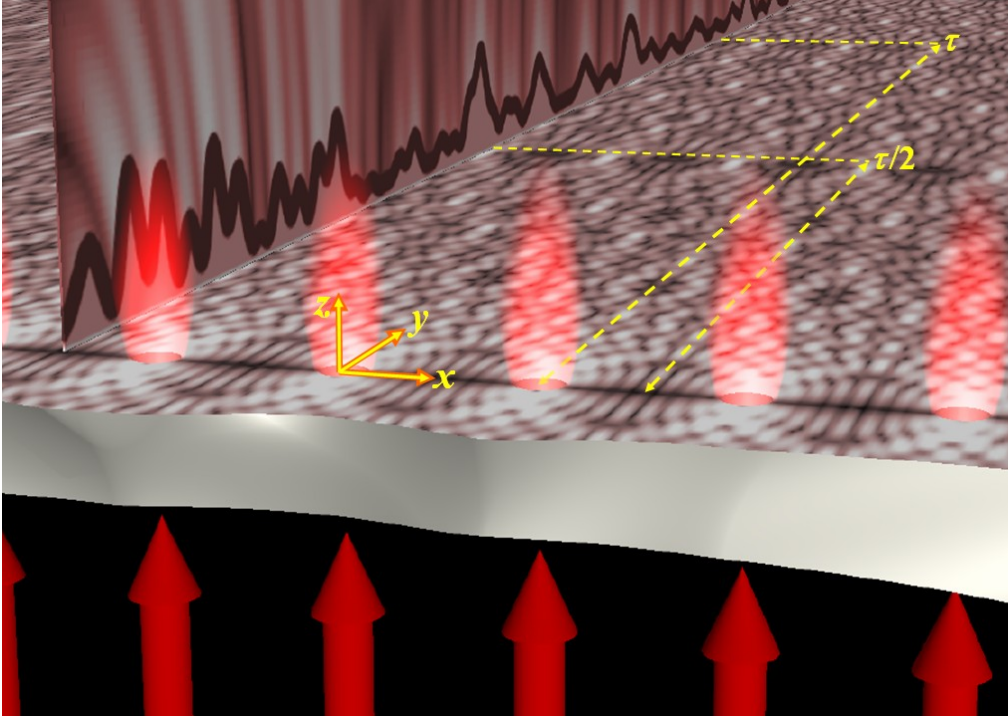


FIG. 1: Illustration of the plasmon Talbot effect above a metal surface. Light is transmitted through a one-dimensional array of nanoholes, setting up a Talbot carpet of interfering plasmon waves. At approximately the Talbot distance  $\tau$  from the array, the propagating plasmons revive, giving an array of plasmon focal spots. Plasmon revival at half that distance is also observed, with the foci displaced by half the period along the array direction. The dependence of the field on height  $z$  above the metal is also shown, with the intensity of the  $z$  component of the plasmons at fixed height superimposed. The carpet plotted is as for Fig. 2(b).

(the  $y$  direction). Therefore, to maximize the observable effect, we choose to make the periodic dipole array in the  $x$  direction, with the plasmons propagating in  $y$ .

The ideal plasmon Talbot field comes from an infinite sum of single dipole fields of the form of Eq. (6), with positions at  $\mathbf{R}_n = (na, 0, 0)$ . Using the Poisson sum formula [24],  $\sum_n \exp(ik_x na) = (2\pi/a) \sum_m \delta(k_x - 2\pi m/a)$ , the infinite sum can be rewritten as a Rayleigh expansion,

$$\begin{aligned} \mathbf{E}_{\text{total}}(\mathbf{r}) &= \frac{2\pi}{a} \sum_m \exp(i2\pi mx/a) \int dk_y \exp(ik_y y + ik_z z) \mathbf{F}(\mathbf{Q}_m) \\ &= \sum_m \exp(i2\pi mx/a) \mathbf{F}_m(y, z), \end{aligned} \quad (8)$$

where in the first line  $\mathbf{Q}_m = (2\pi m/a, k_y)$ , and  $\mathbf{F}(\mathbf{Q})$  is defined in Eq. (7). In the second line,  $2\pi/a$  times the integral has been written as the  $y$ - and  $z$ -dependent Fourier coefficient  $\mathbf{F}_m(y, z)$ . Numerical evaluation of this field, for the values of the parameters above and various choices of  $a$  are shown in Fig. 2(a-c).

For  $a = \lambda_{\text{SP}}$ , the Talbot effect is not yet developed, although an interesting periodic pattern appears that could be employed to imprint high-quality 2D arrays. When we move to larger spacing [ $a = 5\lambda_{\text{SP}}$  in Fig. 2(b)], clear evidence of self-imaging is observed, which is particularly intense at half the Talbot distance. With even larger spacing [ $a = 20\lambda_{\text{SP}}$  in Fig. 2(c)] a fine Talbot carpet is deployed, showing structures reminiscent of cusp caustics at  $\tau$  and  $\tau/2$  [25]. The focal-spot intensities decrease with distance from the hole array due to plasmon attenuation ( $\approx 1.26$  mm for silver at  $\lambda_0 = 1.55 \mu\text{m}$ ), to which image contrast is however insensitive at these low-absorption levels.

The plasmon intensity in the vicinity of slightly less than half the paraxial Talbot distance is shown in Fig. 3 for the same conditions as in Fig. 2(c). The plot on the left shows the field intensity of a focal spot, with cross sectional intensities represented on the right. The lateral width of the spot is  $\approx 0.5\lambda_{\text{SP}}$ , whereas its extension along  $y$  is considerably larger. This type of behavior is also observed for other values of the period and for spots at integer Talbot distances. The width along  $x$  varies from case to case, but it is always close to half a wavelength.

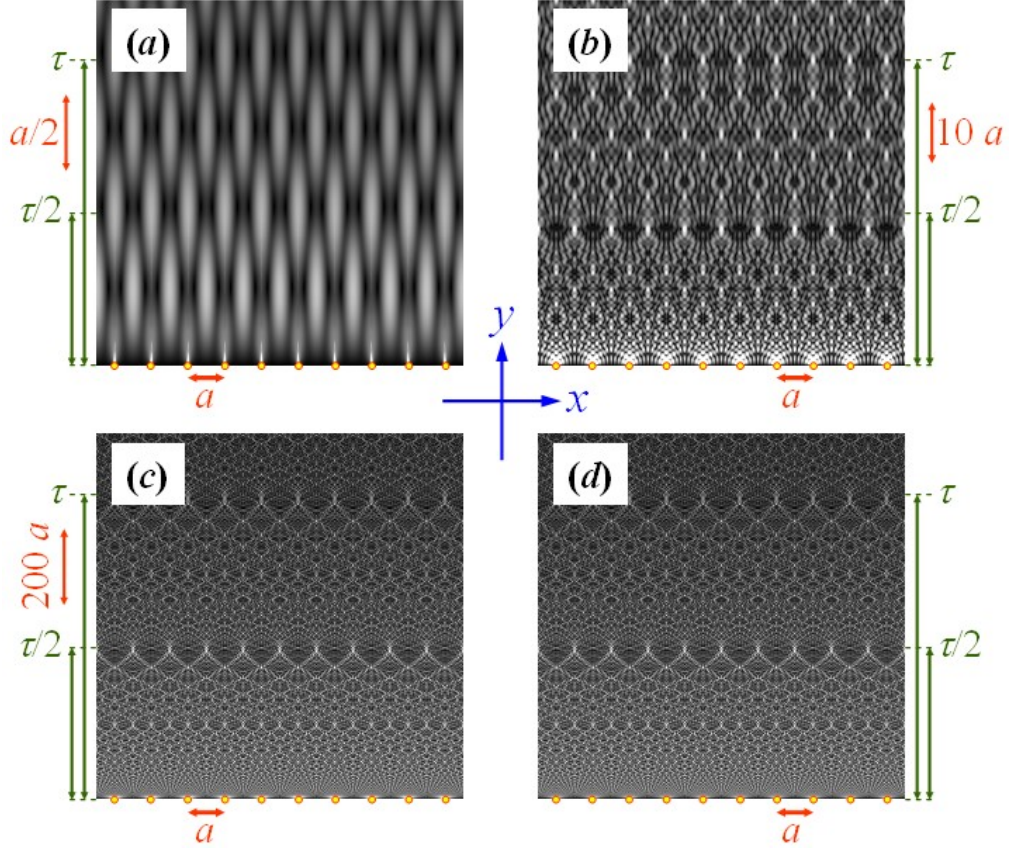


FIG. 2: Plasmon Talbot carpets, numerically computed (a-c) from Eqs. (7)-(8) and analytically approximated (d) from Eqs. (7) and (9) for different choices of the lattice spacing  $a$ : (a)  $a = \lambda_{\text{SP}}$ ; (b)  $a = 5 \lambda_{\text{SP}}$ ; (c,d)  $a = 20 \lambda_{\text{SP}}$ . The amplitude of the  $E_z$  component of the plasmon field is plotted at a height  $z = 0.5 \mu\text{m}$  over a silver surface for a free-space wavelength  $\lambda_0 = 1.55 \mu\text{m}$ , with  $\lambda_{\text{SP}} = 1.544 \mu\text{m}$  the surface plasmon wavelength. Different scales along horizontal and vertical directions are used in each plot: horizontal double arrows show the period  $a$ , while vertical arrows signal the paraxial Talbot distance  $\tau = 2a^2/\lambda_{\text{SP}}$  (long arrows) and half that distance (short arrows). The hole array is represented by circles in the lower part of each plot. The incident light wavevector is along  $z$  and its polarization along  $y$  (see axes in the center of the figure).

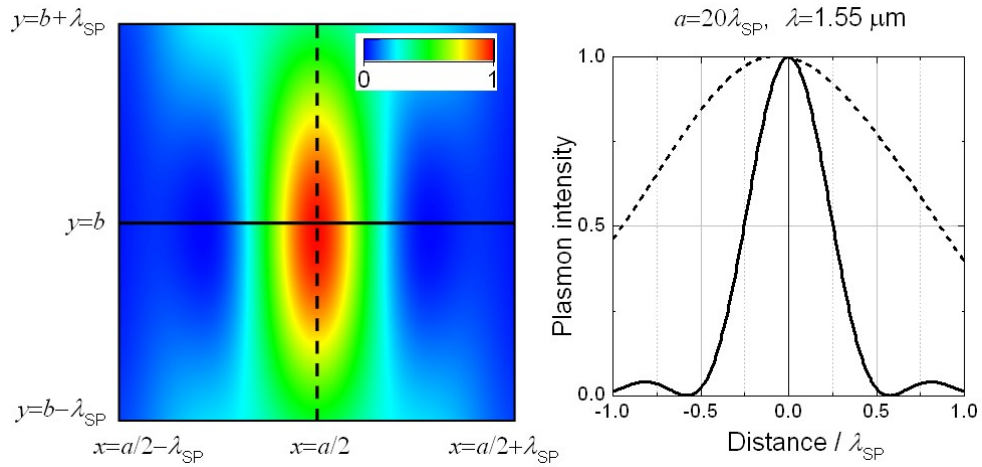


FIG. 3: Shape of a plasmon focal spot near half the Talbot distance in Fig. 2(c). The contour plot (left) shows a square of side  $2\lambda_{\text{SP}}$  centered at  $(x, y) = (a/2, b)$ , with  $a = 20\lambda_{\text{SP}}$  and  $b = \tau/2 - 5\lambda_{\text{SP}} = 395\lambda_{\text{SP}}$ . Plasmon intensities at cross sections of the spot are given on the right along directions parallel (solid curve) and perpendicular (broken curve) with respect to the hole array.



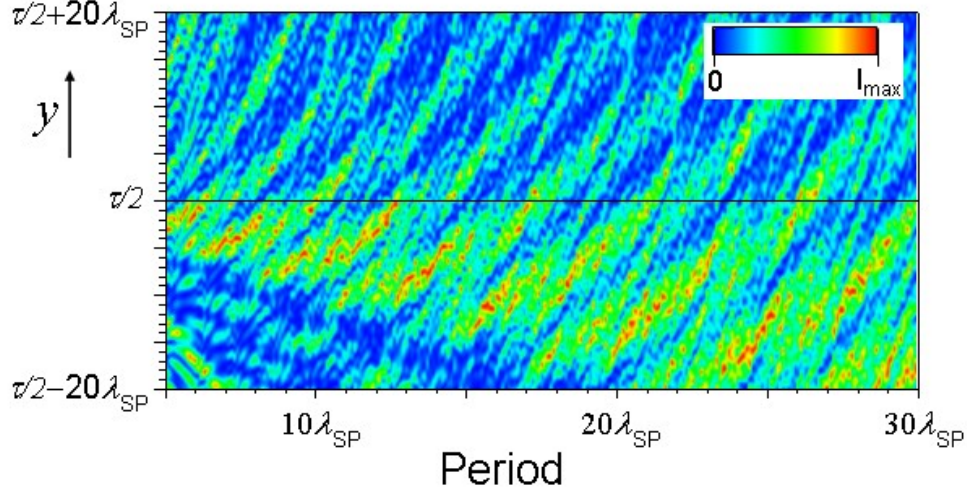


FIG. 4: Lattice-period dependence of the intensity near half the Talbot distance at  $x = a/2$  –in the paraxial Talbot effect [Eq. (3)] the focal spot occurs at exactly  $y = \tau/2$ . The plasmon intensity is represented along  $y$  (vertical axis) as a function of lattice period  $a$  at a height  $z = 0.5 \mu\text{m}$  over a silver surface for a free-space wavelength  $\lambda_0 = 1.55 \mu\text{m}$ . The intensity is normalized to the maximum within the plotted range of  $y$  for each period.

### ANALYTICAL APPROACH

It is possible to approximate the field of Eq. (8) analytically from the observation that the main contribution to the integral over  $k_y$ , particularly in the plasmon far-field, comes from the pole of the  $r_p$  reflection coefficient, in the  $Q$  upper-half complex plane. After all, the plasmon dispersion relation derives from that pole (i.e.,  $\epsilon k_z + k'_z = 0$ ), so that the plasmon itself possesses  $p$  symmetry. This contribution may be approximated by the Cauchy integral theorem using the  $r_p$  plasmon pole of wavenumber  $Q_{SP} = k\sqrt{\epsilon/(\epsilon+1)}$ , corresponding to real plasmon wavelength  $\lambda_{SP} = 2\pi/\Re\{Q_{SP}\}$  [22]. The remaining  $z$  component of the wavevector is  $k_{z,SP} = \sqrt{k^2 - Q_{SP}^2} = k/\sqrt{1+\epsilon}$ . The approximation of the integral by the pole residue is appropriate with a cutoff on the Fourier sum in  $|m| \leq N$ , where  $N \approx a/\lambda_{SP}$ . For  $m$  in this range, the approximation gives

$$\mathbf{F}_m(y, z) \approx \frac{2\lambda_0(2\pi)^3\epsilon^2}{a(\epsilon+1)^2(\epsilon-1)} \exp\left(\frac{ikz}{\sqrt{\epsilon+1}}\right) \exp(iQ_{SP}\zeta_m y) \left(-m\frac{\lambda_0}{a}\frac{\sqrt{\epsilon+1}}{\epsilon}, \frac{-\zeta_m}{\sqrt{\epsilon}}, 1\right), \quad (9)$$

where  $\zeta_m = \sqrt{1 - (2\pi m/aQ_{SP})^2}$ . This analytical expression yields the same structure as Eq. (1), and therefore the general explanation of the Talbot effect offered in Sec. applies here as well (assuming that the imaginary part of  $Q_{SP}$  is small enough to be neglected), apart from the extreme non-paraxiality of the regime under consideration. It should be noted that the  $m$  dependence of  $\mathbf{F}_m$  is only in the vector and in the exponent of  $y$ , and therefore, the Talbot carpet is independent of  $z$  in this plasmon-pole approximation, except for a global exponential decay away from the surface.

The evaluation of Eq. (9) corresponding to the conditions of Fig. 2(c) is plotted in Fig. 2(d). Clearly, the approximation yields excellent results, particularly in the plasmonic far-field. However, the finite cutoff in the Fourier sum implies that there is a finite resolution to all of the interference features in the plasmon field, and hence a finite number of fractional revivals (and obviously no fractal revivals), within a Talbot length.

The choices of the periodicity  $a \leq 20\lambda_{SP}$  in Fig. 2 are in the non-paraxial regime. In Ref. [9], a post-paraxial approximation to the classical Talbot effect was studied, in which Eq. (2) was truncated at the term proportional to  $m^4$ . The inclusion of this and later terms implies that the field is no longer perfectly periodic, and that the distance in  $y$  at which the (imperfect) self-imaging occurs is less than  $\tau$  (as in Fig. 2). However, as our simulations and analytic approximation demonstrate, good, if not perfect, Talbot focusing of plasmons should nevertheless be possible in practice (similar effects have been noticed in free-space propagation [16, 17]). The dependence on the period of the focal spot near  $(x, y) = (a/2, \tau/2)$ , calculated from Eq. (8), is illustrated in Fig. 4, which shows a complex evolution of the spot positions, generally below  $y = \tau/2$ . An interesting consequence of these results is that the position of the focal spot can be controlled through small changes in wavelength.

For very large values of  $|\epsilon|$ , electric dipoles parallel to the metal surface are quenched by their image charges. Then, the transmission through the holes depicted in Fig. 1 relies on parallel magnetic dipoles (provided such dipoles can be

induced, for instance under the condition that the metal skin depth is small compared to the hole size [26]). Magnetic dipoles couple best to plasmons propagating in the  $y$  direction when they are oriented along  $x$ . The above analysis remains valid in that case, and in particular Eq. (9) is only corrected by a factor  $\sqrt{\epsilon + 1}$  multiplying the right-hand side. Normal electric dipoles ( $\parallel \hat{\mathbf{z}}$ ) are also relevant under these conditions, induced by  $p$ -polarized light under oblique incidence. Again, Eq. (9) can be still applied, amended by a factor  $\sqrt{\epsilon}/\zeta_m$ .

## DISCUSSION

Some degree of control over the position of the hot spots is possible when the incident light direction has non-zero projection along the hole array direction  $x$ : the self-image is displaced along  $y$  from the Talbot distance and it is also laterally shifted along  $x$ , as shown both theoretically and experimentally in Ref. [12]. Under these conditions, the projection of the incident light momentum along the hole array,  $k_x^i$ , enters Eq. (9) through an uninteresting overall phase factor, but also through the coefficient of the exponential in  $y$ ,  $Q_{\text{SP}}\zeta_m$ , which becomes  $\sqrt{Q_{\text{SP}}^2 - (2\pi m/a + k_x^i)^2}$ . In the paraxial approximation, one recovers self-imaging at the corrected Talbot distance  $\tau \times (k_{y,\text{SP}}/Q_{\text{SP}})^3$ , where  $k_{y,\text{SP}} = \sqrt{Q_{\text{SP}}^2 - (k_x^i)^2}$ . Simultaneously, the revival is shifted along  $x$  a distance  $y k_x^i/k_{y,\text{SP}}$  that increases with separation from the array. Thus, the position of the focal spots can be controlled through obliquity of the external illumination in a setup as in Fig. 1. One should therefore be able to raster the plasmon focus with nanometer accuracy for potential applications in nanolithography and biosensing.

Controllable plasmon focal spots can be particularly advantageous when combined with recently developed adaptive ultrafast nano-optics [27], in which femtosecond laser pulses are shaped to achieve a desired objective, such as a time-controlled excursion of focal spots in the setup of Fig. 1.

Superoscillating fields with sub-wavelength localization [28] should also be observed with surface plasmon waves using appropriately designed diffraction gratings, as has been recently observed in free-space fields generated by a quasi-crystal array of holes [20].

The analysis presented here can be straightforwardly extrapolated to other types of 2D light waves, such as guided modes in (lossless) dielectric films, long-range surface exciton polaritons [29], or surface modes in patterned perfect-conductor surfaces [30], with interference between metal patterns and Talbot carpets possibly giving rise to unexpected effects in the finer details of the surface modes. The Talbot effect is an attribute of waves, regardless their nature, so it must occur in sound, in elastic waves, and in the more exotic scenario offered by electronic surface states in clean surfaces like Au(111), involving wavelengths in the range of a few nanometers at the Fermi level [31] (e.g., Talbot carpets could be produced in the vicinity of straight-line steps periodically decorated with adhered nanoparticles).

## CONCLUSION

We have described theoretically the surface plasmon analogue to the classical Talbot effect. Our numerical calculation of the dominant normal component agrees well with our analytic approximation in the plasmon far-field. With weak plasmon attenuation, strong focusing of plasmon waves is attainable, even in the non-paraxial regime that we have studied, and some control over the position of this focusing is possible by oblique illumination of the incident optical field.

The plasmonic Talbot effect suggests a straightforward and implementable way of tightly focusing plasmon waves on a metal surface. Despite the lack of perfect self-imaging imposed by the diffraction limit, the focusing is strong enough to allow applications in sensing and imaging. Other potential applications include optical interconnects based upon plasmon focal spots aimed at plasmon waveguides. We have emphasized the simplest case in which the effect should be strongest, namely the normal component of the field emanating from a periodic array of holes on the metal surface. Extensions of the present work to the general case of arbitrary distributions of holes could become an avenue to produce on-demand plasmon fields at far distances from the holes.

## Acknowledgments

This work was supported in part by the Spanish MEC (contract No. NAN2004-08843-C05-05), by the EPSRC (UK), and by the EU (STREP STRP-016881-SPANS and NoE Metamorphose). MRD is supported by the Royal Society of London.

- 
- [1] W. L. Barnes, A. Dereux, and T. W. Ebbesen, *Nature* **424**, 824 (2003).
  - [2] E. Ozbay, *Science* **311**, 189 (2006).
  - [3] R. Zia, J. A. Schuller, A. Chandran, and M. L. Brongersma, *Materials Today* **9**, 20 (2006).
  - [4] J. A. Conway, S. Sahni, and T. Szkopek, *Opt. Express* **15**, 4474 (2007).
  - [5] C. E. Talley, J. B. Jackson, C. Oubre, N. K. Grady, C. W. Hollars, S. M. Lane, T. R. Huser, P. Nordlander, and N. J. Halas, *Nano Lett.* **5**, 1569 (2005).
  - [6] H. F. Talbot, *Philos. Mag.* **9**, 401 (1836).
  - [7] Lord Rayleigh, *Philos. Mag.* **11**, 196 (1881).
  - [8] K. Paturski, *Prog. Opt.* **27**, 1 (1989).
  - [9] M. V. Berry and S. Klein, *J. Mod. Opt.* **43**, 2139 (1996).
  - [10] A. W. Lohmann and D. E. Silva, *Opt. Commun.* **2**, 413 (1971).
  - [11] A. W. Lohmann, *Optik* **79**, 41 (1988).
  - [12] M. Testorf, J. Jahns, N. A. Khilo, and A. M. Goncharenko, *Opt. Commun.* **129**, 167 (1996).
  - [13] K. O'Holleran, M. J. Padgett, and M. R. Dennis, *Opt. Express* **14**, 3039 (2006).
  - [14] I. S. Averbukh and N. F. Perelman, *Phys. Lett. A* **139**, 449 (1989).
  - [15] M. V. Berry, *J. Phys. A* **29**, 6617 (1996).
  - [16] E. Noponen and J. Turunen, *Opt. Commun.* **98**, 132 (1993).
  - [17] T. Saastamoinen, J. Tervo, P. Vahimaa, and J. Turunen, *J. Opt. Soc. Am. A* **21**, 1424 (2004).
  - [18] W. D. Montgomery, *J. Opt. Soc. Am.* **57**, 772 (1967).
  - [19] A. W. Lohmann, H. Knuppertz, and J. Jahns, *J. Opt. Soc. Am. A* **22**, 1500 (2005).
  - [20] F. M. Huang, N. Zheludev, Y. Chen, and F. J. García de Abajo, *Appl. Phys. Lett.* **90**, 091119 (2007).
  - [21] P. B. Johnson and R. W. Christy, *Phys. Rev. B* **6**, 4370 (1972).
  - [22] G. W. Ford and W. H. Weber, *Phys. Rep.* **113**, 195 (1984).
  - [23] J. D. Jackson, *Classical Electrodynamics* (Wiley, New York, 1999).
  - [24] W. Rudin, *Real and Complex Analysis* (McGraw-Hill, London, 1941).
  - [25] M. V. Berry and E. Bodenschatz, *J. Mod. Opt.* **46**, 349 (1999).
  - [26] F. J. García de Abajo, *Rev. Mod. Phys.* (in press).
  - [27] M. Aeschlimann, M. Bauer, D. Bayer, T. Brixner, F. J. García de Abajo, W. Pfeiffer, M. Rohmer, C. Spindler, and F. Steeb, *Nature* **446**, 301 (2007).
  - [28] M. V. Berry and S. Popescu, *J. Phys. A* **39**, 6965 (2006).
  - [29] F. Yang, J. R. Sambles, and G. W. Bradberry, *Phys. Rev. Lett.* **64**, 559 (1990).
  - [30] R. Ulrich and M. Tacke, *Appl. Phys. Lett.* **22**, 251 (1972).
  - [31] A. Mugarza, A. Mascaraque, V. Pérez-Dieste, V. Repain, S. Rousset, F. J. García de Abajo, and J. E. Ortega, *Phys. Rev. Lett.* **87**, 107601 (2001).